

# On-Chip Chiral Mode Switching by Encircling an Exceptional Point in an Anti-Parity-Time Symmetric System

Weiwei Liu, Yicong Zhang, Zhihua Deng, Jianghua Ye, Kai Wang, Bing Wang,\*  
Dingshan Gao,\* and Peixiang Lu\*

Dynamically encircling the exceptional point (EP) of an anti-parity-time (anti-PT) symmetric system can achieve chiral mode switching between symmetry-broken eigenmodes, which is especially important for developing nanophotonic devices. However, the realization of anti-PT-symmetric systems on a chip still remains significantly challenging as precisely controlling the parameters of nanophotonic structures is difficult. Herein, a novel anti-PT-symmetric system is designed and constructed on a silicon-on-insulator chip by taking advantage of subwavelength gratings to help engineer nanophotonic structures. Consequently, on-chip chiral switching between symmetry-broken eigenmodes is experimentally realized by dynamically encircling the EP in parametric space of the proposed anti-PT-symmetric system. Moreover, the achieved chiral mode switching exhibits high output power ratios ( $\geq 6.4$  dB) at 1550 nm, wide-band response that covers C-band completely, and great thermal stability up to 90 °C, which indicate desirable performance features for practical applications in optical communication. This study paves an avenue for realizing on-chip chiral switching between symmetry-broken modes, which shows great promise for developing nanophotonic devices, such as optical switching, logic gates, and isolators, in optical telecommunication bands.

associated eigenvectors coalesce simultaneously; such singularities are called exceptional points (EPs).<sup>[1–8]</sup> In particular, a system will experience a phase transition as parameters dynamically evolve around EPs,<sup>[9–14]</sup> thus inducing various fascinating phenomenon and applications, such as electromagnetically induced transparency,<sup>[15]</sup> unidirectional invisibility,<sup>[16–19]</sup> laser mode selectivity,<sup>[20–22]</sup> and sensitivity enhancement.<sup>[23–28]</sup> More interestingly, adiabatically encircling an EP in parametric space can result in a topological phase transfer between the eigenstates of a system, i.e., the output mode is determined only by the encircling direction rather than the input mode. For example, in parity-time (PT) symmetric systems with Hamiltonians satisfying  $[PT, H_{PT}] = 0$ ,<sup>[2,9,29–32]</sup> dynamically encircling the corresponding EPs causes asymmetric mode switching between symmetric-phase eigenstates (symmetric and antisymmetric modes), which has been demonstrated in microwave and

## 1. Introduction

Nonconservative systems with gain/loss can be described by non-Hermitian Hamiltonians. In contrast to conventional Hermitian systems, non-Hermitian systems exhibit branch point singularities in parameter space, where eigenvalues and the


optical telecommunication bands.<sup>[33–37]</sup> Moreover, a recent surge has been observed in attempts to investigate the asymmetric mode transfer in coupled microcavities, photonic crystals, and nonlinear waveguides, laying significant foundations for realizing versatile and functional nanophotonic devices; for example, directional lasing,<sup>[38,39]</sup> surface-enhanced chiral detection,<sup>[40]</sup> and tunable vortex radiation.<sup>[41]</sup>

More recently, anti-PT-symmetric systems<sup>[42–44]</sup> have attracted significant attention for light steering in cold atoms,<sup>[45]</sup> nonlinear microcavity,<sup>[8,46]</sup> and synthetic photonic lattice.<sup>[47–49]</sup> Since the features of an anti-PT-symmetric system are conjugated to PT-symmetric counterparts,<sup>[50,51]</sup> adiabatically encircling an EP in an anti-PT-symmetric system results in a chiral mode transfer between symmetry-broken eigenstates displayed as the localized modes in separated components. This has been realized in the microwave domain using coupled yttrium iron garnet strips.<sup>[52]</sup> Since symmetry-broken modes correspond to the input and output of integrated photonic devices, implementing on-chip chiral switching between symmetry-broken modes is especially promising for developing functional nanophotonic devices in optical telecommunication bands, including optical switching, logic gates, and isolators. However, this implementation remains

W. Liu, Y. Zhang, Z. Deng, J. Ye, K. Wang, B. Wang, D. Gao, P. Lu  
Wuhan National Laboratory for Optoelectronics and School of Physics  
Huazhong University of Science and Technology  
Wuhan, Hubei 430074, China  
E-mail: wangbing@hust.edu.cn; dsgao@hust.edu.cn;  
lupeixiang@hust.edu.cn

W. Liu, Y. Zhang, Z. Deng, J. Ye, K. Wang, B. Wang, D. Gao, P. Lu  
Optics Valley Laboratory  
Wuhan, Hubei 430074, China

P. Lu  
Hubei Key Laboratory of Optical Information and Pattern Recognition  
Wuhan Institute of Technology  
Wuhan, Hubei 430205, China

 The ORCID identification number(s) for the author(s) of this article can be found under <https://doi.org/10.1002/lpor.202100675>

DOI: 10.1002/lpor.202100675

challenging, limited by the difficulty in precisely controlling the propagation loss and effective index in a nanophotonic structure.

In this study, on-chip chiral mode switching between symmetry-broken modes is investigated at optical communication wavelengths. Subwavelength gratings (SWGs) can accurately control the propagation loss and effective index of nanophotonic structures,<sup>[36,53,54]</sup> offering an ideal platform to realize non-Hermitian nanophotonic systems. Based on silicon-on-insulator (SOI) SWGs, an on-chip anti-PT-symmetric system is designed and constructed to steer light propagation by dynamically encircling an EP in parametric space. Consequently, the aforementioned chiral switching is experimentally demonstrated, i.e., the final output is determined only using encircling direction, regardless of input states. Moreover, the achieved on-chip chiral mode switching exhibits high output power ratios ( $\geq 6.4$  dB) between the desired mode and counterpart at 1550 nm, wide-band response, and great thermal stability up to 90 °C, which are desirable performance metrics for optical communication.

## 2. Theoretical Model

Anti-PT symmetry requires dissipative coupling between bare components, which is difficult to implement in real-space photonic systems. Herein, the adiabatic elimination technique is used to introduce imaginary coupling into non-Hermitian systems.<sup>[52,55,56]</sup> Considering a non-Hermitian photonic system comprising three coupled waveguides, the amplitudes of eigenmodes in each waveguide  $a_{1,2,3}(z)$  can be calculated through the coupled-mode equation

$$-i \frac{d}{dz} \begin{bmatrix} a_1(z) \\ a_2(z) \\ a_3(z) \end{bmatrix} = \begin{bmatrix} \beta_1 & \kappa_1 & 0 \\ \kappa_1 & \beta_2 + i\Gamma & \kappa_2 \\ 0 & \kappa_2 & \beta_3 \end{bmatrix} \begin{bmatrix} a_1(z) \\ a_2(z) \\ a_3(z) \end{bmatrix} \quad (1)$$

where  $\beta_{1,2,3}$  stand for the propagating constants of individual waveguides, and  $\Gamma$  represents the propagation loss of middle waveguide. The coupling coefficients between adjacent waveguides are denoted as  $\kappa_1$  and  $\kappa_2$ . Moreover, the next-neighbor coupling between waveguide 1 (WG1) and waveguide 3 (WG3) can be neglected. As waveguide 2 (WG2) plays the role of link waveguide, an indirect dissipative coupling exists between WG1 and WG3. To adiabatically eliminate the  $a_2(z)$  term in Equation (1), the conditions  $\beta_2 = (\beta_1 + \beta_3)/2$  and  $|\kappa_{1,2}| \ll 1$  must be satisfied. For simplicity, the effective modal indices  $\alpha_{1,2,3} = \beta_{1,2,3}/k_0$  are used in forthcoming equations, where  $k_0$  is the propagation constant in vacuum. Correspondingly, the coupling coefficient and propagation loss can be expressed as  $C_{1,2} = \kappa_{1,2}/k_0$  and  $\gamma = \Gamma/k_0$ , respectively. Thus, the Hamiltonian can be written as

$$H = \begin{bmatrix} \alpha_1 & C_1 & 0 \\ C_1 & \alpha_2 + i\gamma & C_2 \\ 0 & C_2 & \alpha_3 \end{bmatrix} \quad (2)$$

Under the conditions  $\Delta\alpha/2 \ll \gamma$  ( $\Delta\alpha = \alpha_3 - \alpha_1$ ) and  $|C_{1,2}| \ll \gamma$ , an equivalent 2x2 Hamiltonian matrix can be acquired to de-

scribe the anti-PT-symmetric system (see Section S1, Supporting Information)

$$H_{\text{eq}} = \begin{bmatrix} \alpha_2 - \frac{\Delta\alpha}{2} + i\frac{C_1^2}{\gamma} & i\frac{C_1 C_2}{\gamma} \\ i\frac{C_1 C_2}{\gamma} & \alpha_2 + \frac{\Delta\alpha}{2} + i\frac{C_2^2}{\gamma} \end{bmatrix} \quad (3)$$

The eigenvalues of the equivalent anti-PT-symmetric system are solved as

$$E_{1,3} = \alpha_2 + \frac{i(C_1^2 + C_2^2) \mp \sqrt{(\Delta\alpha\gamma)^2 - (C_1^2 + C_2^2)^2 - 2i\Delta\alpha\gamma(C_1^2 - C_2^2)}}{2\gamma} \quad (4)$$

Equation (4) indicates that the eigenvalues of the Hamiltonian  $H_{\text{eq}}$  are generally complex, but they coalesce at

$$C_1 = C_2 = \sqrt{\frac{|\Delta\alpha|\gamma}{2}} = C_{\text{EP}} \quad (5)$$

which denotes the EP. For  $C_1 = C_2 = C < C_{\text{EP}}$ , the imaginary parts of eigenvalues coalesce. The corresponding eigenvectors take the form

$$|\varphi_{1,3}\rangle = \begin{bmatrix} i \left( \pm \sqrt{(\Delta\alpha\gamma)^2 - 4C^4 - \Delta\alpha\gamma} \right) \\ 1, \frac{2C^2}{2C^2} \end{bmatrix}^T \quad (6)$$

indicating that the energies of eigenmode 1 and eigenmode 3 are dominantly distributed in WG1 and WG3, respectively, which represent the symmetry-broken phase. For  $C_1 = C_2 = C > C_{\text{EP}}$ , the real parts of eigenvalues coalesce, and the corresponding eigenvectors can be expressed as

$$|\varphi_{1,3}\rangle = \begin{bmatrix} \mp \sqrt{4C^4 - (\Delta\alpha\gamma)^2 - i\Delta\alpha\gamma} \\ 1, \frac{2C^2}{2C^2} \end{bmatrix}^T \quad (7)$$

which describes the symmetric phase. In addition, to realize chiral mode switching by adiabatically encircling EP, the starting/end point of encircling loop must lie in the symmetry-broken phase, which is significantly different from PT-symmetric systems.<sup>[35]</sup>

## 3. Results and Discussions

### 3.1. Design of On-Chip Anti-PT-Symmetric System

To accurately control the propagation loss and effective index of waveguides, SWGs are adopted to construct an on-chip anti-PT-symmetric system (Figure 1a) based on a standard SOI platform with a 220 nm thick top silicon layer. Compared with the conventional method of introducing propagation loss by adding metals on silicon waveguides, the utilization of SWG waveguides avoids the complicated nanofabrication procedure in which the overlay process is inevitably adopted.<sup>[57–59]</sup> The designed wavelength

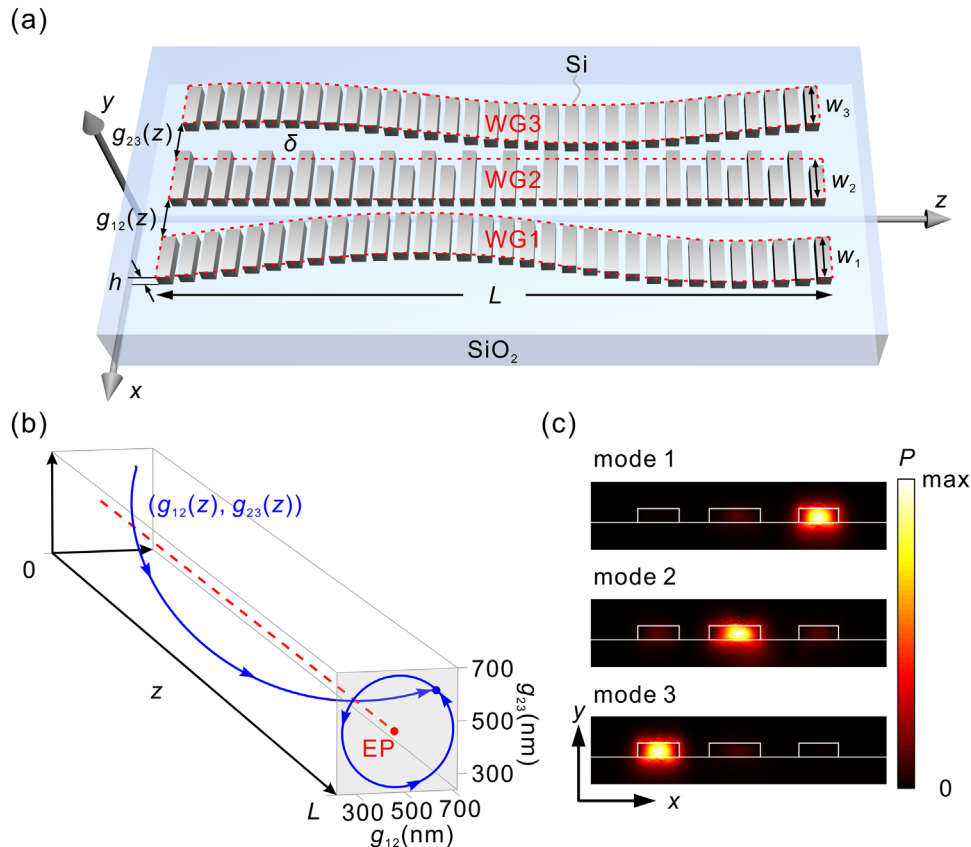


**Figure 1.** Design of the anti-PT-symmetric system based on SWG waveguides. a) Schematic of the SWG waveguides system. The red dashed lines mark the continuous boundaries of SWGs, which define gaps. b) The encircling loop in parameter space. The blue and red dots mark the starting/end point and EP, respectively. c) The power distributions of the three eigenmodes at the input/output ports of waveguides.

is 1550 nm, corresponding to the central wavelength of C-band for optical communication. The period of SWGs is fixed as  $\Lambda = 300$  nm, and the filling factor is set as  $f = 0.565$ . To ensure that only the fundamental transverse electric (TE) mode is allowed in the waveguides with height  $h = 220$  nm, the widths of WG1 and WG3 are set as  $w_1 = 655$  nm and  $w_3 = 675$  nm, respectively. The corresponding effective modal indices are calculated as  $\alpha_1 = 1.548$  and  $\alpha_3 = 1.570$  (see Section S2, Supporting Information), which guarantee that the approximate condition  $\alpha_1 \approx \alpha_3$  is satisfied and that Equation (3) suits the system. The average width of WG2 is set as  $w_2 = 705$  nm with an effective modal index of  $\alpha_2 = 1.559$ . Note that a periodic corrugation of WG2 is necessarily accompanied by introducing propagation loss, due to the scattering of propagating light. The loss coefficient is determined as  $\gamma = 0.0254$  for a corrugating amplitude  $\delta = 130$  nm. According to Equation (4), the parameter space for dynamically encircling comprises the coupling coefficients  $C_1$  and  $C_2$ , which are associated with the gap between WG1 and WG2 ( $g_{12}$ ) as well as the gap between WG2 and WG3 ( $g_{23}$ ), respectively. The coupling coefficient as a function of gap is presented in Figure S3a (see Section S2, Supporting Information). The position of EP, characterized by the relation in Equation (5), is determined to be at  $(g_{12}, g_{23}) = (460, 470)$  nm. As light propagates from  $z = 0$  to  $z = L$ , the parametric variation causes an encircling loop around the EP in  $(g_{12}, g_{23})$  plane. To satisfy the condition that the starting/end point of

loop is located in the symmetry-broken phase ( $C_1 = C_2 < C_{EP}$ ), the encircling loop is designed as  $g_{12}(z) = 472 + 230 \cos(2\pi z/L + \pi/4)$  nm and  $g_{23}(z) = 470 + 210 \sin(2\pi z/L + \pi/4)$  nm, where the length of waveguides  $L$  is set as  $70.2 \mu\text{m}$  to guarantee an adiabatic evolution of parameters.<sup>[36,60,61]</sup>

Figure 1b shows the evolution routing in parameter space and the corresponding encircling loop in  $(g_{12}, g_{23})$  plane, where encircling in the counterclockwise (CCW) and clockwise (CW) directions correspond to propagating along  $+z$  and  $-z$ , respectively. Figure 1c presents the power distributions of eigenmodes for the coupled waveguide system, which characterize typical symmetry-broken eigenmodes as dominantly localized in individual waveguides. The modes with energy dominantly localized in WG1, WG2, and WG3 are denoted as mode 1, mode 2, and mode 3, respectively. According to Equation (3), the equivalent model of a waveguide doublet comprising WG1 and WG3 with a dissipative coupling coefficient is used to study chiral mode switching. To manifest the evolution process in theory, the eigenvalues of the equivalent Hamiltonian  $H_{eq}$  and the corresponding evolution trajectories are calculated according to the designed encircling loop, as illustrated in Figure 2 (see Section S3, Supporting Information for the corresponding imaginary parts). The green (red) sheets of Riemann surfaces represent the eigenvalue with a lower (higher) imaginary part. The eigenvalue with a lower real part is identical to mode 1, and the other is identical to mode 3. The state of the

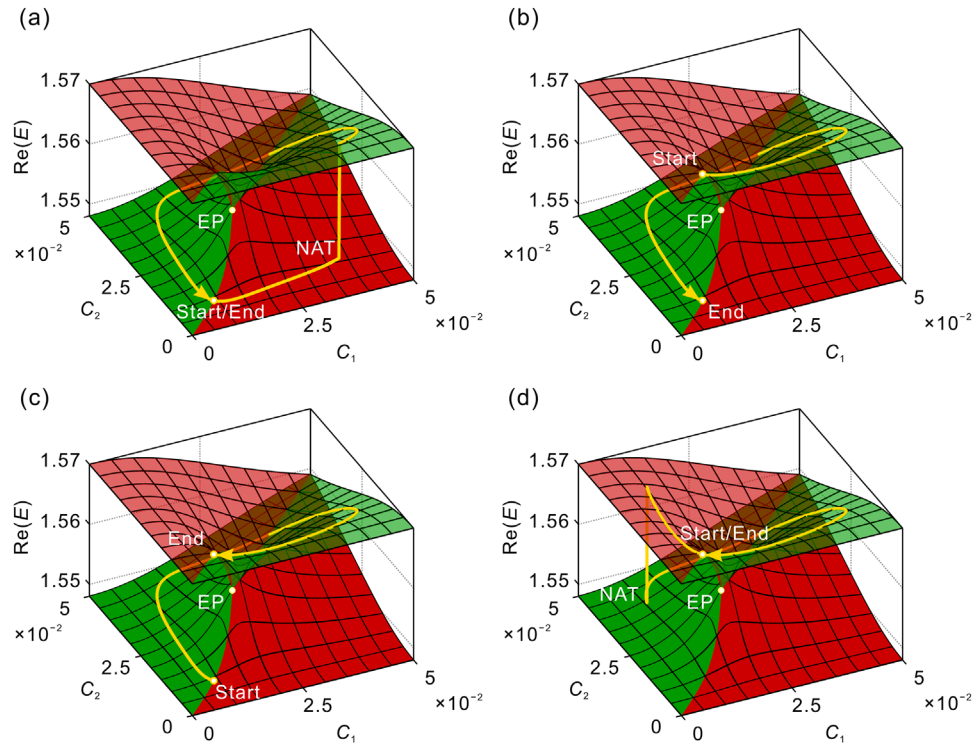


**Figure 2.** Riemann sheets of the real parts of eigenvalues in  $(C_1, C_2)$  space. The green and red sheets represent the eigenvalues with lower and higher imaginary parts (i.e., the mode with lower and higher loss), respectively. The yellow curves show the trajectories corresponding to the encircling loop in Figure 1b for the cases: a) injection with mode 1 for CCW encircling loop, b) injection with mode 3 for CCW encircling loop, c) injection with mode 1 for CW encircling loop, and d) injection with mode 3 for CW encircling loop.

equivalent waveguide doublet can be expanded as a linear superposition of two eigenstates

$$|\psi(z)\rangle = c_1(z)|\varphi_1(z)\rangle + c_2(z)|\varphi_2(z)\rangle \quad (8)$$

where the subscripts 1 and 2 represent the eigenstates with lower and higher losses, respectively. The amplitude coefficients  $c_{1,2}$  can be solved based on the equivalent Hamiltonian in Equation (3). The trajectories are plotted on the green (red) sheet for  $|c_1| > |c_2|$  ( $|c_1| < |c_2|$ ), indicating that the eigenmode with the lower (higher) loss dominates in waveguides. In particular, nonadiabatic transition (NAT) occurs when the state is on the unstable higher-loss Riemann sheet.<sup>[35,62]</sup> Figure 2a,b illustrates the evolution process for CCW encircling loop. Initially, incidence with mode 1 results in an evolution trajectory on the higher-loss sheet (Figure 2a). As the state is unstable, it jumps to the lower-loss sheet due to NAT, indicating that symmetry-broken mode 1 is still maintained till the end. However, incidence with mode 3 is significantly different as the entire trajectory is located on the lower-loss Riemann sheet (Figure 2b). Consequently, the initial state (mode 3) is gradually transferred to the other eigenstate (mode 1). Figure 2c,d shows the evolution trajectories for CW encircling loop in which mode 1 and mode 3, respectively, are injected at  $z = L$ . A similar result can be obtained in that mode 3 is always the final output regardless of the initial state. To summarize, the output mode is only determined by the encircling direction, which ensures chiral behavior for the mode switching between symmetry-broken modes.

### 3.2. Experimental Realization of On-Chip Chiral Mode Switching

For experimental realization, SWG arrays are utilized to fabricate the anti-PT-symmetric system on an SOI chip, which offers a convenient approach for precisely controlling propagation loss and effective index. SWG arrays are fabricated through electron beam lithography (EBL) and inductively coupled plasma (ICP) etching of an SOI substrate (see Section S4.1, Supporting Information). Figure 3a presents the top-view scanning electron microscopy (SEM) images of the fabricated SWG arrays. The whole morphology indicates that the elements of SWG arrays are uniformly distributed on the SOI chip. In particular, the periodically corrugated structure in WG2 is clearly identifiable. The enlarged parts show that the unit cells of SWGs have a regular and smooth surface. The fabricated nanophotonic structures agree well with the planned design, suggesting the realization of a three-waveguide-coupled anti-PT-symmetric system on an SOI chip.

The transmission properties of the prepared three-waveguide-coupled anti-PT-symmetric system are measured. The light from a broadband amplified spontaneous emission (ASE) source is coupled to one of the SWGs with a 2D grating coupler (see Section S4.2, Supporting Information). In practice, the localized eigenmodes of individual SWGs can be approximately regarded as the corresponding symmetry-broken modes of coupled SWG waveguides (Figure 1c). Figure 3b displays the measured modal transmittance ( $T_{mn}$ ) from WG $m$  into WG $n$  ( $m, n = 1, 3$ ) for CCW encircling, as a function of wavelength. Note that the transmittance  $T_{m1}$  is always significantly larger than the transmittance

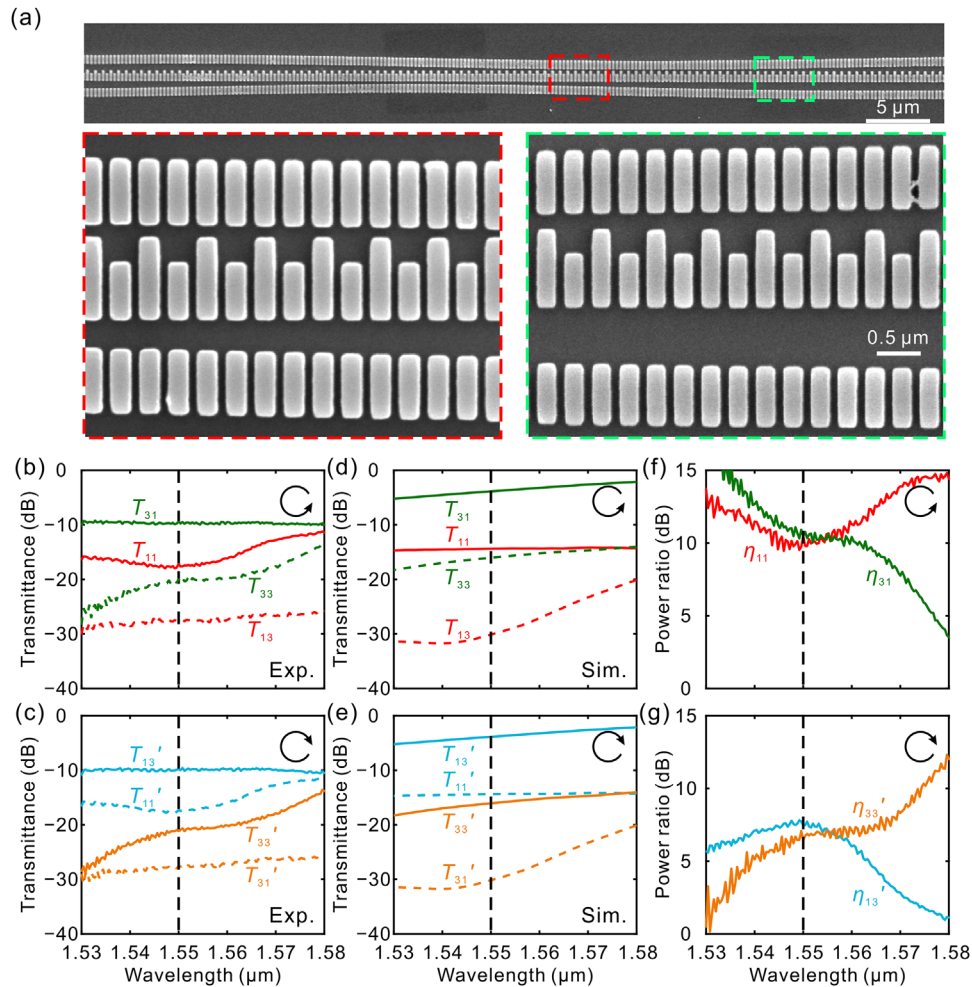


**Figure 3.** Structure of the on-chip anti-PT-symmetric system based on SWG waveguides as well as experimental and simulated results of chiral mode switching. a) SEM images of the fabricated SWG waveguides and enlarged SEM images of the areas marked by the red and green dashed boxes. Experimentally measured transmission spectra for b) CCW and c) CW encircling loops. Numerically calculated transmission spectra for d) CCW and e) CW encircling loops.  $T_{mn}$  ( $T_{mn}'$ ) signifies the transmittance with injections from WG $m$  and output at WG $n$  for propagation along + $z$  (− $z$ ) direction ( $m, n = 1, 3$ ). The arrows represent the corresponding encircling directions in parameter space. f, g) Logarithmic plots of the power ratio between the output ports for CCW and CW encircling loops, respectively. The black dashed lines mark the designed operating wavelength at 1550 nm.

$T_{m3}$ , indicating that an arbitrary eigenmode injected from the left side ( $z = 0$ ) can be transferred into mode 1 when arriving at the right terminal ( $z = L$ ). In contrast, Figure 3c plots the modal transmittance ( $T_{mn}'$ ) from WG $m$  into WG $n$  ( $m, n = 1, 3$ ) for CW encircling. The transmittance  $T_{m3}'$  is always significantly larger than the transmittance  $T_{m1}'$ , indicating that an arbitrary eigenmode injected from the right side ( $z = L$ ) can be transferred into mode 3 when arriving at the left terminal ( $z = 0$ ). Transmittance spectra is also calculated by numerical simulation, via the finite-difference time-domain (FDTD) method (FDTD Solutions, Lumerical). The structural parameters of the on-chip anti-PT-symmetric system are utilized as designed. The profiles of the calculated transmission spectra are consistent with the experimental results, as shown in Figure 3d,e. The differences in the amplitudes of transmittance can be attributed to the imperfections in fabrication process that cause a redshift in the ideal transmission spectra (see Section S4.3, Supporting Information) and introduce undesirable backscattering, to decrease trans-

mittance. The experimental and calculated results unambiguously demonstrate chiral mode switching between symmetry-broken modes in an anti-PT-symmetric system designed on an SOI chip.

Figure 3f plots the logarithmic power ratio between mode 1 and mode 3 at the output for the CCW encircling loop. Mode 1 dominates at the output terminal with a power ratio  $\eta_{11} = T_{11} - T_{13} = 10.47$  dB for mode 1 incidence and a power ratio  $\eta_{31} = T_{31} - T_{33} = 10.48$  dB for mode 3 incidence at 1550 nm. For the CW encircling loop, Figure 3g shows that mode 3 dominates at the output terminal with a power ratio  $\eta_{13}' = T_{13}' - T_{11}' = 7.5$  dB for mode 1 incidence and a power ratio  $\eta_{33}' = T_{33}' - T_{31}' = 6.4$  dB for mode 3 incidence at 1550 nm. Moreover, although the device is designed to operate at 1550 nm, a slight variation in EP location will not affect topological features. Consequently, the device still has a good response for chiral mode switching within a specific wavelength range of 1530–1580 nm, covering the full C-band for optical communication (1530–1565 nm).

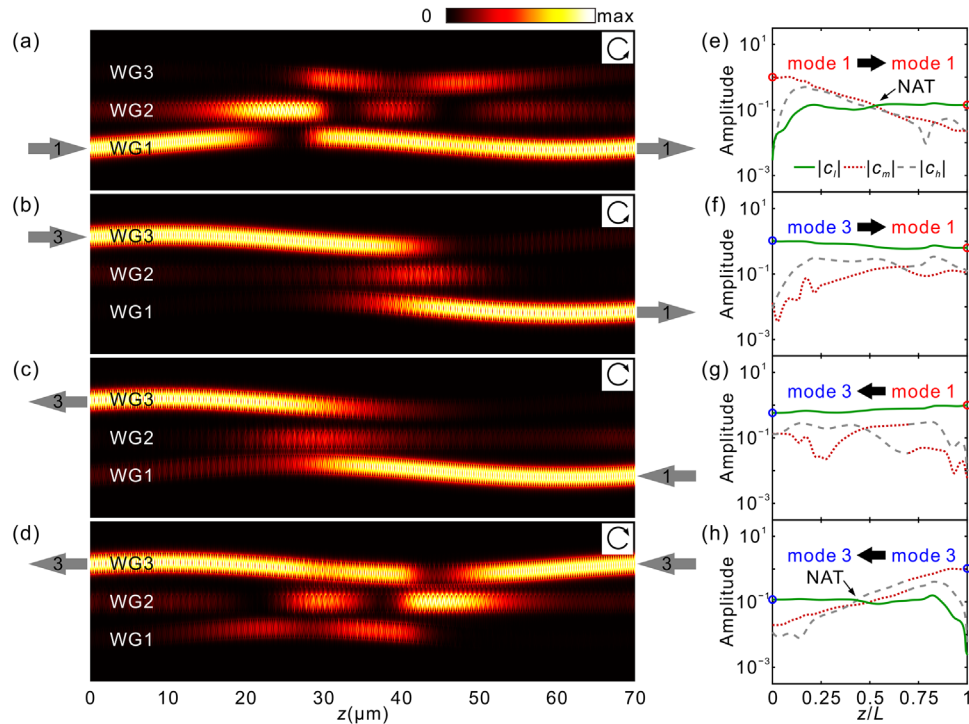


**Figure 4.** Evolution of numerically simulated power profiles and mode amplitudes in SWG waveguides. The power profiles are obtained for: a) injection with mode 1 for CCW encircling loop, b) injection with mode 3 for CCW encircling loop, c) injection with mode 1 for CW encircling loop, and d) injection with mode 3 for CW encircling loop. The power profiles are normalized along the propagation direction to distinctly reveal the mode transfer process. The arrows at the ends of waveguides mark the input and output modes. e–h) Corresponding amplitudes of instantaneous modes in the evolution process.

### 3.3. Numerical Simulations

Chiral mode switching between symmetry-broken modes in the on-chip anti-PT-symmetric system is simulated using FDTD (see Section S4.4, Supporting Information). **Figure 4a,b** shows the power profiles in  $+z$  direction (CCW encircling loop) with the symmetry-broken eigenmodes injected from WG1 and WG3, respectively. The obtained field distributions are normalized with regards to the incident power for evidently displaying mode transfer. Notably, regardless of injected eigenmodes, the flow of light always tends to output at the end of WG1. In contrast, for the flow of light in  $-z$  direction (CW encircling loop), the final state is always localized in WG3 (Figure 4c,d). Therefore, the numerical calculation further demonstrates the asymmetric switching between symmetry-broken modes in the anti-PT-symmetric system constructed on the SOI chip, which agrees well with the proposed design and the corresponding experimental results.

Mode amplitudes are calculated as functions of propagation distance to reveal the evolution dynamics of eigenmodes in practical three-waveguide-coupled system. The field distribution of system at an arbitrary propagation distance can be expressed as the superposition of all eigenmodes

$$|\psi(z)\rangle = c_l(z)|\varphi_l(z)\rangle + c_m(z)|\varphi_m(z)\rangle + c_h(z)|\varphi_h(z)\rangle \quad (9)$$

where the subscripts l, m, and h mark the instantaneous eigenmodes with the lowest, moderate, and highest losses, respectively. The evolution of amplitude coefficients  $|c_l|$  (green curve),

$|c_m|$  (red curve), and  $|c_h|$  (grey curve) corresponding to the four cases are plotted in Figure 4e–h. The dominated modes at the input and output ports of waveguides are marked with red (mode 1) and blue (mode 3) circles, respectively. Note that although mode 1 and mode 3 at the starting/end point share approximately equal losses, the relative loss levels of the two modes on each side of the imaginary-part coalescence line in parametric space are opposite (see Section S5, Supporting Information). To elaborate, mode 1 suffers a lower loss for  $C_1 < C_2$ , while mode 3 suffers a lower loss for  $C_1 > C_2$ . Therefore, the lowest-loss mode (green curve) is identical to mode 1 for propagation along  $+z$  direction (CCW encircling) and is identical to mode 3 for propagation along  $-z$  direction (CW encircling), when approaching the output terminal. For CCW encircling, Figure 4e shows that  $|c_m|$  dominates initially as mode 1 is injected, but it becomes smaller than  $|c_l|$  due to NAT. Consequently, the mode with the lowest loss starts to dominate after NAT, which corresponds to mode 1 at the output terminal. In contrast, Figure 4f shows that NAT is absent as mode 3 is injected, indicating that the process is completely adiabatic. Therefore,  $|c_l|$  dominates the whole process, and the incident mode 3 is transferred into mode 1 in this situation. In Figure 4g,h, opposite evolutions can be observed for CW encircling. As mode 1 is injected, NAT is absent and the incident mode 1 is transferred into mode 3. As mode 3 is injected, the output state does not change due to NAT. Note that the curves of  $|c_m|$  and  $|c_h|$  are disconnected in the vicinity of  $z = 0.7L$  (Figure 4e–h), which is attributed to the exchange in the relative losses of two corresponding eigenmodes (see Section S5, Supporting Information). Overall, in all the four

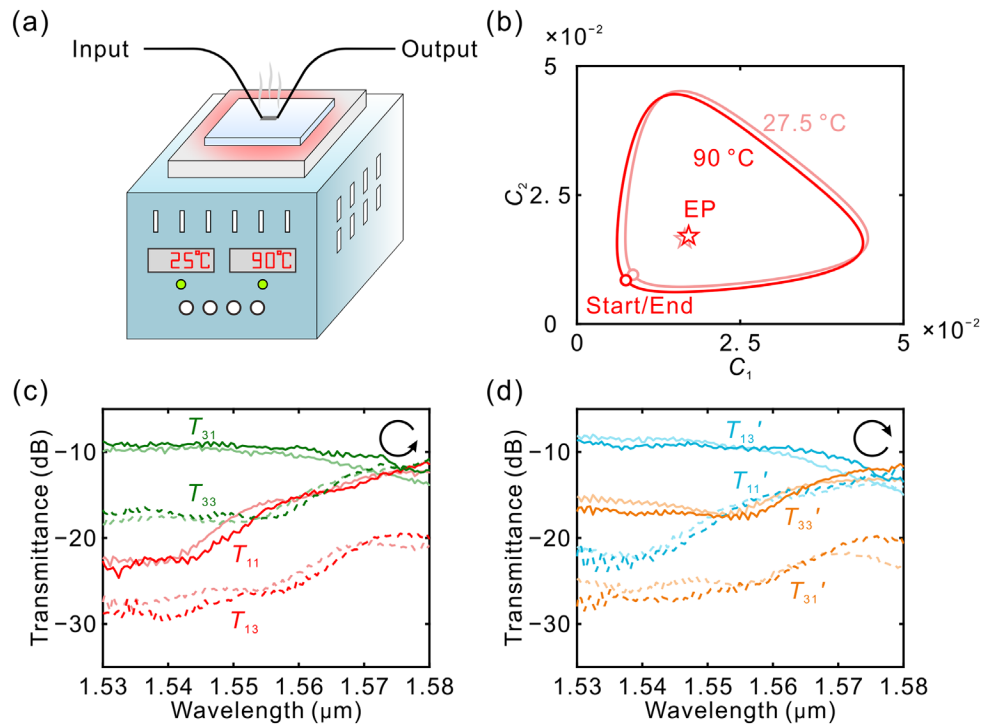


**Figure 5.** Demonstration of the thermal stability of on-chip chiral switching. a) Schematic of the experimental setup for thermal stability measurements. b) The encircling loops in  $(C_1, C_2)$  space at room temperature (27.5 °C) and high temperature (90 °C). The starting/end points and EPs are marked by circles and stars, respectively. Experimentally measured transmission spectra at 27.5 °C (light colors) and 90 °C (dark colors) for c) CCW and d) CW encircling loops.

cases,  $|c_1(z)|$  is always the largest near the output, indicating that the system tends to evolve toward the most stable state during adiabatic parameter evolution.<sup>[35,63]</sup> Moreover, the experimental and simulated results demonstrate that the anti-PT-symmetric model described by Equation (3) has opened an avenue for designing on-chip nanophotonic devices to realize chiral mode switching between symmetry-broken modes.

### 3.4. Demonstration of the Thermal Stability of On-Chip Chiral Switching

The thermal stability of integrated devices is important for operating at high temperatures.<sup>[64]</sup> To investigate the high-temperature response of chiral mode switching in the on-chip anti-PT-symmetric system, the fabricated device is positioned on a hotplate for heating, as shown in Figure 5a. The target high temperature is set as 90 °C to avoid damaging the silicon chip seriously. As reported, the thermo-optic effect increases the refractive index of silicon with increasing temperature.<sup>[65]</sup> The thermo-optical coefficient of silicon around 1550 nm is  $\approx 1.86 \times 10^{-4} \text{ K}^{-1}$ , indicating that the refractive index of silicon waveguide will increase by  $\Delta n = dn/dT \cdot \Delta T = 0.012$ .<sup>[65]</sup> Figure 5b plots the encircling loops at room temperature (27.5 °C) and high temperature (90 °C). The increase in temperature slightly influences the evolution trajectory, demonstrating the robustness of the fabricated device against temperature. For further analysis, transmission spectra are measured for comparison, as shown in Figure 5c,d for

CCW and CW encircling loops, respectively. Note that the transmission spectra measured at 90 °C are approximately the same as that measured at room temperature. Therefore, the chiral switching between symmetry-broken modes is immune to the perturbations induced by the thermo-optic effect at a high temperature, indicating an excellent thermal stability of the nanophotonic devices fabricated based on an SOI chip.

## 4. Conclusion

In this study, a novel on-chip anti-PT-symmetric system is realized for achieving chiral switching between symmetry-broken modes. SWGs provide an ideal platform to construct the proposed anti-PT-symmetric system on an SOI chip. The proposed design achieves the aforementioned chiral mode switching by dynamically encircling the EP in parametric space. Moreover, metrics, such as high output power ratios ( $\geq 6.4$  dB) between the desired mode and the counterpart at 1550 nm, wide-band response covering C-band completely, and great thermal stability up to 90 °C, are achieved, indicating desirable performance features for practical applications in optical communication. This work opens an avenue for realizing an anti-PT-symmetric system, which will further promote the exploration of novel nanophotonic non-Hermitian systems. Furthermore, the proposed subwavelength designs can integrate with other nanophotonic devices on a single chip, showing great promise for realizing optical interconnections in optical telecommunication bands.

## Supporting Information

Supporting Information is available from the Wiley Online Library or from the author.

## Acknowledgements

W.L., Y.Z., and Z.D. contributed equally to this work. The work was supported by the National Natural Science Foundation of China (Grant Nos. 11974124, 11804109, 12021004, and 61975062). The authors gratefully acknowledged the Center of Micro-Fabrication and Characterization (CMFC) of WNLO (HUST) for their support in the nanofabrication (EBL and ICP) of devices.

## Conflict of Interest

The authors declare no conflict of interest.

## Data Availability Statement

The data that support the findings of this study are available from the corresponding author upon reasonable request.

## Keywords

anti-parity-time symmetric systems, chiral mode switching, exceptional points, non-Hermitian, silicon-on-insulator

Received: November 25, 2021

Revised: August 16, 2022

Published online:

- [1] W. D. Heiss, *J. Phys. A: Math. Theor.* **2012**, *45*, 444016.
- [2] Ş. K. Özdemir, S. Rotter, F. Nori, L. Yang, *Nat. Mater.* **2019**, *18*, 783.
- [3] M.-A. Miri, A. Alù, *Science* **2019**, *363*, eaar7709.
- [4] C. Wang, R. S. Williams, A. D. Stone, L. Yang, *Science* **2021**, *373*, 1261.
- [5] M. Parto, Y. G. N. Liu, B. Bahari, M. Khajavikhan, D. N. Christodoulides, *Nanophotonics* **2021**, *10*, 403.
- [6] H.-Z. Chen, T. Liu, H.-Y. Luan, R.-J. Liu, X.-Y. Wang, X.-F. Zhu, Y.-B. Li, Z.-M. Gu, S.-J. Liang, H. Gao, L. Lu, L. Ge, S. Zhang, J. Zhu, R.-M. Ma, *Nat. Phys.* **2020**, *16*, 571.
- [7] W. Liu, Y. Wu, C.-K. Duan, X. Rong, J. Du, *Phys. Rev. Lett.* **2021**, *126*, 170506.
- [8] A. Roy, S. Jahani, Q. Guo, A. Dutt, S. Fan, M.-A. Miri, A. Marandi, *Optica* **2021**, *8*, 415.
- [9] R. El-Ganainy, K. G. Makris, M. Khajavikhan, Z. H. Musslimani, S. Rotter, D. N. Christodoulides, *Nat. Phys.* **2018**, *14*, 11.
- [10] L. Feng, R. El-Ganainy, L. Ge, *Nat. Photonics* **2017**, *11*, 752.
- [11] H. Zhao, L. Feng, *Natl. Sci. Rev.* **2018**, *5*, 183.
- [12] S. H. Park, L. Sung-Gyu, S. Baek, T. Ha, S. Lee, M. Bumki, S. Zhang, M. Lawrence, T.-T. Kim, *Nanophotonics* **2020**, *9*, 1031.
- [13] Q. Zhong, M. Khajavikhan, D. N. Christodoulides, R. El-Ganainy, *Nat. Commun.* **2018**, *9*, 4808.
- [14] H. Nasari, G. Lopez-Galmitche, H. E. Lopez-Aviles, A. Schumer, A. U. Hassan, Q. Zhong, S. Rotter, P. LiKamWa, D. N. Christodoulides, M. Khajavikhan, *Nature* **2022**, *605*, 256.
- [15] C. Wang, X. Jiang, G. Zhao, M. Zhang, C. W. Hsu, B. Peng, A. D. Stone, L. Jiang, L. Yang, *Nat. Phys.* **2020**, *16*, 334.
- [16] X. Yin, X. Zhang, *Nat. Mater.* **2013**, *12*, 175.
- [17] L. Feng, Y.-l. Xu, W. S. Fegadolli, M.-h. Lu, J. E. B. Oliveira, V. R. Almeida, Y.-f. Chen, A. Scherer, *Nat. Mater.* **2013**, *12*, 108.
- [18] Z. Lin, H. Ramezani, T. Eichelkraut, T. Kottos, H. Cao, D. N. Christodoulides, *Phys. Rev. Lett.* **2011**, *106*, 213901.
- [19] Y. Huang, Y. Shen, C. Min, S. Fan, G. Veronis, *Nanophotonics* **2017**, *6*, 977.
- [20] M. Brandstetter, M. Liertzer, C. Deutsch, P. Klang, J. Schöberl, H. E. Türeci, G. Strasser, K. Unterrainer, S. Rotter, *Nat. Commun.* **2014**, *5*, 4034.
- [21] E. Lafalce, Q. Zeng, C. H. Lin, M. J. Smith, S. T. Malak, J. Jung, Y. J. Yoon, Z. Lin, V. V. Tsukruk, Z. V. Vardeny, *Nat. Commun.* **2019**, *10*, 561.
- [22] H. Hodaei, M.-A. Miri, M. Heinrich, D. N. Christodoulides, M. Khajavikhan, *Science* **2014**, *346*, 975.
- [23] H. Hodaei, A. U. Hassan, S. Wittek, H. Garcia-Gracia, R. El-Ganainy, D. N. Christodoulides, M. Khajavikhan, *Nature* **2017**, *548*, 187.
- [24] W. Chen, Ş. Kaya Özdemir, G. Zhao, J. Wiersig, L. Yang, *Nature* **2017**, *548*, 192.
- [25] Z. Xiao, H. Li, T. Kottos, A. Alù, *Phys. Rev. Lett.* **2019**, *123*, 213901.
- [26] J. Wiersig, *Nat. Commun.* **2020**, *11*, 2454.
- [27] Y. Wu, P. Zhou, T. Li, W. Wan, Y. Zou, *Opt. Express* **2021**, *29*, 6080.
- [28] Q. Zhong, J. Ren, M. Khajavikhan, D. N. Christodoulides, Ş. K. Özdemir, R. El-Ganainy, *Phys. Rev. Lett.* **2019**, *122*, 153902.
- [29] K. G. Makris, R. El-Ganainy, D. N. Christodoulides, Z. H. Musslimani, *Phys. Rev. Lett.* **2008**, *100*, 103904.
- [30] C. M. Bender, S. Boettcher, *Phys. Rev. Lett.* **1998**, *80*, 5243.
- [31] C. E. Rüter, K. G. Makris, R. El-Ganainy, D. N. Christodoulides, M. Segev, D. Kip, *Nat. Phys.* **2010**, *6*, 192.
- [32] A. Regensburger, C. Bersch, M.-A. Miri, G. Onishchukov, D. N. Christodoulides, U. Peschel, *Nature* **2012**, *488*, 167.
- [33] J. Doppler, A. A. Mailybaev, J. Böhm, U. Kuhl, A. Girschik, F. Libisch, T. J. Milburn, P. Rabl, N. Moiseyev, S. Rotter, *Nature* **2016**, *537*, 76.
- [34] J. W. Yoon, Y. Choi, C. Hahn, G. Kim, S. H. Song, K.-Y. Yang, J. Y. Lee, Y. Kim, C. S. Lee, J. K. Shin, H.-S. Lee, P. Berini, *Nature* **2018**, *562*, 86.
- [35] X.-L. Zhang, S. Wang, B. Hou, C. T. Chan, *Phys. Rev. X* **2018**, *8*, 021066.
- [36] Q. Liu, S. Li, B. Wang, S. Ke, C. Qin, K. Wang, W. Liu, D. Gao, P. Berini, P. Lu, *Phys. Rev. Lett.* **2020**, *124*, 153903.
- [37] Y. Zhang, W. Liu, H. Long, K. Wang, B. Wang, P. Lu, *Opt. Express* **2021**, *29*, 44146.
- [38] B. Peng, Ş. K. Özdemir, M. Liertzer, W. Chen, J. Kramer, H. Yilmaz, J. Wiersig, S. Rotter, L. Yang, *Proc. Natl. Acad. Sci. USA* **2016**, *113*, 6845.
- [39] S. I. Azzam, K. Chaudhuri, A. Lagutchev, Z. Jacob, Y. L. Kim, V. M. Shalaev, A. Boltasseva, A. V. Kildishev, *Laser Photonics Rev.* **2021**, *15*, 2000411.
- [40] T. Wu, W. Zhang, H. Zhang, S. Hou, G. Chen, R. Liu, C. Lu, J. Li, R. Wang, P. Duan, J. Li, B. Wang, L. Shi, J. Zi, X. Zhang, *Phys. Rev. Lett.* **2020**, *124*, 083901.
- [41] W. E. Hayenga, M. Parto, J. Ren, F. O. Wu, M. P. Hokmabadi, C. Wolff, R. El-Ganainy, N. A. Mortensen, D. N. Christodoulides, M. Khajavikhan, *ACS Photonics* **2019**, *6*, 1895.
- [42] S. Longhi, *Opt. Lett.* **2018**, *43*, 4025.
- [43] Y. Li, Y.-G. Peng, L. Han, M.-A. Miri, W. Li, M. Xiao, X.-F. Zhu, J. Zhao, A. Alù, S. Fan, C.-W. Qiu, *Science* **2019**, *364*, 170.
- [44] P. Peng, W. Cao, C. Shen, W. Qu, J. Wen, L. Jiang, Y. Xiao, *Nat. Phys.* **2016**, *12*, 1139.
- [45] Y. Jiang, Y. Mei, Y. Zuo, Y. Zhai, J. Li, J. Wen, S. Du, *Phys. Rev. Lett.* **2019**, *123*, 193604.
- [46] F. Zhang, Y. Feng, X. Chen, L. Ge, W. Wan, *Phys. Rev. Lett.* **2020**, *124*, 053901.
- [47] A. Bergman, R. Duggan, K. Sharma, M. Tur, A. Zadok, A. Alù, *Nat. Commun.* **2021**, *12*, 486.
- [48] Y. Dai, Z. Wen, K. Ji, Z. Liu, H. Wang, Z. Zhang, Y. Gao, B. Lu, Y. Wang, X. Qi, J. Bai, *Opt. Lett.* **2020**, *45*, 3099.



- [49] S. Ke, D. Zhao, J. Liu, Q. Liu, Q. Liao, B. Wang, P. Lu, *Opt. Express* **2019**, *27*, 13858.
- [50] J. Wen, X. Jiang, L. Jiang, M. Xiao, *J. Phys. B: At., Mol. Opt. Phys.* **2018**, *51*, 222001.
- [51] H. Qi, X. Hu, X. Wang, Q. Gong, *Phys. Rev. A* **2021**, *103*, 063520.
- [52] X.-L. Zhang, T. Jiang, C. T. Chan, *Light: Sci. Appl.* **2019**, *8*, 88.
- [53] Y. Wang, Z. Lu, M. Ma, H. Yun, F. Zhang, N. A. F. Jaeger, L. Chrostowski, *IEEE Photonics J.* **2016**, *8*, 7101408.
- [54] P. Cheben, R. Halir, J. H. Schmid, H. A. Atwater, D. R. Smith, *Nature* **2018**, *560*, 565.
- [55] M. Mrejen, H. Suchowski, T. Hatakeyama, C. Wu, L. Feng, K. O'Brien, Y. Wang, X. Zhang, *Nat. Commun.* **2015**, *6*, 7565.
- [56] A. Hashemi, S. M. Rezaei, S. K. Özdemir, R. El-Ganainy, *APL Photonics* **2021**, *6*, 040803.
- [57] G. Roelkens, D. Van Thourhout, R. Baets, *Opt. Express* **2006**, *14*, 11622.
- [58] M. Pan, H. Zhao, P. Miao, S. Longhi, L. Feng, *Nat. Commun.* **2018**, *9*, 1308.
- [59] A. Guo, G. J. Salamo, D. Duchesne, R. Morandotti, M. Volatier-Ravat, V. Aimez, G. A. Siviloglou, D. N. Christodoulides, *Phys. Rev. Lett.* **2009**, *103*, 093902.
- [60] T. J. Milburn, J. Doppler, C. A. Holmes, S. Portolan, S. Rotter, P. Rabl, *Phys. Rev. A* **2015**, *92*, 052124.
- [61] A. Li, J. Dong, J. Wang, Z. Cheng, J. S. Ho, D. Zhang, J. Wen, X.-L. Zhang, C. T. Chan, A. Alù, C.-W. Qiu, L. Chen, *Phys. Rev. Lett.* **2020**, *125*, 187403.
- [62] Y. Choi, J. W. Yoon, J. K. Hong, Y. Ryu, S. H. Song, *Commun. Phys.* **2020**, *3*, 140.
- [63] X.-L. Zhang, C. T. Chan, *Commun. Phys.* **2019**, *2*, 63.
- [64] G.-W. Lu, J. Hong, F. Qiu, A. M. Spring, T. Kashino, J. Oshima, M.-a. Ozawa, H. Nawata, S. Yokoyama, *Nat. Commun.* **2020**, *11*, 4224.
- [65] H. H. Li, *J. Phys. Chem. Ref. Data* **1980**, *9*, 561.